SOLUTAL NATURAL CONVECTION FLOWS IN TERNARY MIXTURES

Jordi Pallares[1*], Josefina Gavaldà[2], Xavier Ruiz[2,3]

[1]Departament d'Enginyeria Mecànica, Universitat Rovira i Virgili, Av. Països Catalans, 26, 43007-Tarragona. Spain.

[2]Departament de Química Física i Inorgànica, Universitat Rovira i Virgili, C/ Marcel·lí Domingo s/n, 43007-Tarragona. Spain

[3]Institut d'Estudis Espacials de Catalunya, C/ Gran Capità, 2-4, 08034 Barcelona. Spain

[*]Corresponding author: e-mail: jordi.pallares@urv.cat, Tel. +34 977 559 682, Fax. +34 977 559 691

ABSTRACT

It is known that the cross diffusion terms generate four different types of solutions to the one-dimensional unsteady diffusion equations for ternary mixtures. The stability of the fluid column corresponding to these solutions can be classified depending on the sign of the first derivative of density with respect to the direction of the gravity vector (i.e. $\partial\rho/\partial y$) and the sign of $(\partial^2\rho/\partial y^2)/y$, where $y = 0$ is located at the center of the diffusion layer. The type of solution depends on the initial conditions and on the set of diffusion coefficients considered. One type of solution corresponds to a stable fluid column with ($\partial\rho/\partial y < 0$) and $(\partial^2\rho/\partial y^2)/y > 0$. Two types of solutions generate fluid layers with unstable density stratification ($\partial\rho/\partial y > 0$) and the fourth type shows a fluid layer with $(\partial^2\rho/\partial y^2)/y < 0$. We analyzed the unsteady diffusion processes in a ternary mixture under the conditions of experiments carried out to determine the four diffusion coefficients of the the ternary system 1,2,3,4-tetrahydronaphthaline-isobutylbenzene-dodecane (THN-IBB-nC12). These measurements; performed in diffusion cells with an initially stable stratification within the cell, with the denser mixture at the bottom and the lighter at the top; are usually based on the validity of the one-dimensional unsteady diffusion mass transfer equations. The linear stability analysis for the onset of convection in the unstable layers with unstable density stratification ($\partial\rho/\partial y > 0$) indicates that the critical thickness of these layers depends on the Rayleigh numbers, on the diffusion coefficients and on the initial conditions. To illustrate the flow structures that can be generated in these unstable conditions, we performed numerical simulations for selected sets of diffusion coefficients at different Rayleigh numbers. The results of these simulations are in general agreement with the predictions of the linear stability analysis and indicate that, under specific conditions, the convective motions developed in the cell produce significant departures of the concentration distributions from the pure diffusion situation.

Keywords: natural convection, solutal convection, diffusion coefficient, cross diffusion, ternary mixtures, linear stability, numerical simulation.

NOMENCLATURE

a	wavenumber
D	diffusion coefficient
g	gravitational acceleration
K_e	kinetic energy
L	characteristic length
p	pressure
$\Re$	real part
Ra	Rayleigh number
Sc	Schmidt number
t	time
u_i	velocity components
w	mass fraction
x, y, z	Cartesian coordinates

Greek letters

β	solutal expansion coefficient, $\beta_i = (\partial\rho/\partial w_i)/\rho_{(0,0)}$
δ_{ij}	Kronecker's delta
δ	layer thickness
Δ	increment
η	similarity variable
λ	wavelegth
μ	dynamic viscosity
ν	kinematic viscosity

ρ	density
ψ	streamfuction

Subscripts and superscripts

$*$	non-dimensional
$1, 2, 3$	component of the mixture
b	basic state
bot	value at the bottom of the cell
c	critical
in	initial value
o	reference value
top	value at the top of the cell

Special characters

$\bar{\ }$	averaged on a horizontal plane
$\langle\ \rangle$	volume averaged
$'$	perturbation

1-INTRODUCTION

The experimental determination of the mass diffusion and thermodiffusion coefficients of the different chemical species in multicomponent liquid systems is relevant in many scientific and technological applications related, for instance, with crystal growth or biological systems [1-4]. Additionally, mass diffusion and thermodiffusion has due to the geothermal gradient, important implications in Earth sciences and, in particular, in petroleum industry. In this case, a more precise understanding of thermodiffusion phenomena can result in a more accurate modeling of crude oil reservoirs, which can lead to the reduction of the number of wells required and the cost of the initial prospections [5-7].

The present study considers liquid mixtures at room temperature -isothermal conditions- and to the particular ternary mixture of 1,2,3,4-tetrahydronaphthaline (THN), isobutylbenzene (IBB) and n-dodecane (nC12). This mixture is considered as a representative model of the different molecular families of the oil in natural reservoirs. Specifically, the naphthalenic, aromatic and aliphatic compounds are associated with the THN, IBB and nC_{12}, respectively. Due to this similarity this particular system has been extensively investigated in Earth laboratories and also in reduced gravity environments, as the FOTON M3 spacecraft [8] or the International Space Station (ISS). In this last case, the corresponding experimental campaign of the European Space Agency, named Diffusion and Soret Coefficients-Diffusion Coefficients in Mixtures (DSC-DCMIX1) was initiated six years ago and many interesting results are still appearing in the literature [9-11].

A common experimental strategy for the determination of the four molecular diffusion coefficients of this transparent ternary system on Earth laboratories and at room temperature consists in the initial introduction of a heavier mixture at the bottom part of a diffusion cell while a lighter one is placed at the top. In this situation of stable stratification, molecular diffusion takes place and the resulting concentration distribution allows the final obtaining of the different terms of the diffusion matrix. In the Counter Flow Cell (CFC) technique [12, 13] optical digital interferometry [14-16] is used to measure the density profile within the mixture. The subsequent nonlinear fitting between the obtained experimental data and the corresponding theoretical profiles of the purely diffusive process allows the obtaining of the four diffusion coefficients [12]. Another methodology, the so-called Sliding Symmetric Tubes (SST) technique, uses a set of large moving tubes of small diameter [17-19]. The measurements and the subsequent nonlinear regressions are based on the determination of the averaged concentration values of the two different species in the upper and lower part of the different tubes [20, 21]. The typical length of the parallelepipedic cell in the CFC method is about one centimeter while that of the cylindrical cell in the SST one is twelve centimeters. This means that the experiments, especially in the second case, are very time consuming. Typically, fifteen-eighteen days for SST against a few hours for CFC. However, despite the apparent simplicity of both methods, there exists in the literature an evident scatter in the numerical values of the diffusion coefficients which indicates some still unsolved difficulties [20].

To help in the resolution of this problem other methodologies have been used in Earth laboratories not only to obtain the diffusion matrix but also the Soret and thermodiffusion coefficients. The most common techniques found in the literature are the Open Ended Capillary Technique (OCT) [22, 23], the Taylor Dispersion Technique (TDT) [24] and the Two-Color Optical Beam Deflection Technique, (OBD) [25]

In addition, to try to avoid the potential effect of residual convection in diffusion cells, the DSC-DCMIX1 experiment has also been performed in the International Space Station. In this case, the determination of the different coefficients was performed using the Selectable Optical Diagnostic Instrument (SODI) installed in the Microgravity Science Glovebox on the U.S. Laboratory, Destiny module [26]. The application of these different measurement techniques and environments to the same mixture shows appreciable scatter of the results, mainly in the values of the secondary diagonal of the diffusion matrix.

In Earth laboratories, a potential source of problems could be the evolution of convective motions in the initially stable flow due to the local competitions of the two driving forces generated by the concentration gradients of both independent components [27-29]. The result of this competition generates, in some cases, double-diffusive instabilities which could be appreciable perturbations in the experimental determination of the four molecular diffusion coefficients [30-33].

In summary, the present study particularizes and analyzes, theoretically and numerically, the possibility of the onset of undesired solutal natural convection flows in diffusion experiments of the ternary mixture THN-IBB-nC_{12} used in the DSC-DCMIX1 experiment. The flow structures that may develop and their potential effect on the determination of the diffusion coefficients are also reported and in deep discussed.

2.-MODELING DETAILS

The THN-IBB-nC_{12} ternary mixture at constant room temperature is enclosed in a small parallelepipedic cell with rigid walls. Figure 1 shows the geometry used, which coincides with the one reported in the literature to determine the mass diffusion coefficients of the above-mentioned ternary mixture [12, 13].

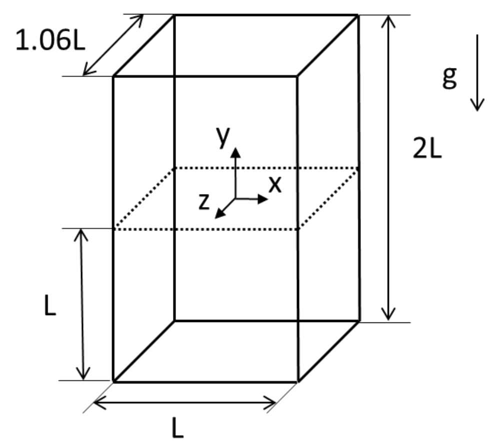

Figure 1. Sketch of a diffusion cell used in the determination of diffusion coefficients [12] and the coordinate system adopted.

The density of the mixture as a function of the concentrations can be modeled as, [17, 19]

$$\rho = \rho_0[1 + \beta_1(w_1 - \overline{w}_1) + \beta_2(w_2 - \overline{w}_2)] \quad (1)$$

where w_1 and w_2 are the local mass fractions of THN and IBB, respectively, $\overline{w}_1$ and $\overline{w}_2$ are the volume averaged mass fractions, $\rho_0 = 842.377\ kg\ m^{-3}$, $\beta_1 = 0.2581$ and $\beta_2 = 0.1370$, which are valid for mass fractions ratios close to 1:1:1. The dynamic viscosity of the mixture is considered constant (μ=1.289·10^{-3}Pa·s) [17].

2.1.-*Unsteady one-dimensional pure diffusion*

Assuming a ternary mixture of constant physical properties and a purely unsteady one-dimensional diffusion, the dimensionless mass transport equations can be written as

$$\frac{\partial w_1}{\partial t^*} = \frac{\partial^2 w_1}{\partial y^{*2}} + D_{12}^* \frac{\partial^2 w_2}{\partial y^{*2}} \tag{2}$$

$$\frac{\partial w_2}{\partial t^*} = D_{22}^* \frac{\partial^2 w_2}{\partial y^{*2}} + D_{21}^* \frac{\partial^2 w_1}{\partial y^{*2}} \tag{3}$$

The length scale used to define the non-dimensional variables is the width L and, since the self diffusion coefficient of component 1, D_{11}, is positive, the time scale is L^2/D_{11}. Using these scales, the dimensional diffusion coefficients are scaled with D_{11} (i.e. $D_{ij}^* = D_{ij}/D_{11}$)

Analytical solutions of Eqs. 2 and 3, for an infinite domain, are summarized in Appendix A. The form of these closed solutions excludes some combinations of the diffusion coefficients which lead to non-physical (non-real) solutions for the mass fractions of the components of the mixture. Specifically the following restrictions apply [22, 34]

$$\begin{gathered} D_{11} > 0,\ D_{22} > 0,\ D_{12} \neq 0 \\ D_{11}D_{22} - D_{12}D_{21} > 0 \text{ and } (D_{11} - D_{22})^2 + 4D_{12}D_{21} \ \geq 0 \end{gathered} \tag{4}$$

2.2.-Unsteady three dimensional solutal convective flow

If solutal free convection is considered, the non-dimensional continuity, momentum and mass transfer equations, assuming constant physical properties except for the linear variation of density with the concentration in the buoyancy terms, can be written as,

$$\frac{\partial u_i^*}{\partial x_i^*} = 0 \tag{5}$$

$$\frac{\partial u_i^*}{\partial t^*} + \frac{\partial u_j^* u_i^*}{\partial x_j^*} = -\frac{\partial p^*}{\partial x_i^*} + Sc \frac{\partial^2 u_i^*}{\partial x_j^{*2}} - Ra_1 Sc\, w_1 \delta_{i2} - Ra_2 Sc\, w_2 \delta_{i2} \tag{6}$$

$$\frac{\partial w_1}{\partial t^*} + \frac{\partial u_j^* w_1}{\partial x_j^*} = \frac{\partial^2 w_1}{\partial x_j^{*2}} + D_{12}^* \frac{\partial^2 w_2}{\partial x_j^{*2}} \tag{7}$$

$$\frac{\partial w_2}{\partial t^*} + \frac{\partial u_j^* w_2}{\partial x_j^*} = D_{22}^* \frac{\partial^2 w_2}{\partial x_j^{*2}} + D_{21}^* \frac{\partial^2 w_1}{\partial x_j^{*2}} \tag{8}$$

As in Equations 2 and 3, the length and time scales used to define the dimensionless variables are the width L and the diffusion time based on the self-diffusion coefficient of component 1, L^2/D_{11}. In Equation 6, $Sc = \mu/\rho_o\, D_{11}$ is the Schmidt number and $Ra_1 = \beta_1 L^3 g/\nu\, D_{11}$ and $Ra_2 = \beta_2 L^3 g/\nu\, D_{11}$ are the solutal Rayleigh numbers. Note that β_1 and β_2 are defined in Equation 1 and ρ_o is the reference density, $\rho_o = (\rho_{top} + \rho_{bot})/2$.

Non-slip boundary conditions for velocity and zero mass diffusion fluxes are imposed at the six walls of the cell. This last condition is equivalent to set to zero the derivatives of the mass fractions with respect to the wall-normal direction. In addition, the initial conditions assume fluid at rest and initial mass fractions for THN and IBB [13] as,

$$\begin{array}{c} w_{in\,THN}^{top} = w_{in1}^{top} = 0.31996, w_{in\,IBB}^{top} = w_{in2}^{top} = 0.34001 \\ w_{in\,THN}^{bot} = w_{in1}^{bot} = 0.33891, w_{in\,IBB}^{bot} = w_{in2}^{bot} = 0.31991 \end{array} \quad (9)$$

Under these conditions the heavier mixture is placed in the half bottom of the cell and the lighter mixture at the top.

The set of governing equations (Eqs. 5 to 8) together with the corresponding boundary conditions have been solved numerically with a validated domestic code that has been used for the simulation of thermal [35, 36] and solutal [37-39] convective flows. The mass and momentum diffusive fluxes and the momentum convective terms are discretized with second-order centered schemes while the mass advection terms are discretized with the TVD scheme [40]. The momentum equations are integrated in time with the Crank-Nicholson scheme and the mass transfer equations with the second-order explicit Adams-Bashford method. The non-dimensional time step was set to $2{\cdot}10^{-6}$. Simulations were performed with a grid of 55x150x55 nodes. The node distributions are uniform along the horizontal directions ($\Delta x^* = \Delta z^* = 0.018$) and stretched towards $y^* = 0$ along the vertical direction ($\Delta y^*_{max} = 0.022$, $\Delta y^*_{min} = 0.005$). Two simulations were conducted at the two largest Rayleigh numbers considered ($Ra_1 = 1.78 \cdot 10^8$ and $Ra_2 = 9.49 \cdot 10^7$) with finer grids (65x170x65 and 75x190x75). Figure 2 compares the evolutions of the volume averaged kinetic energy of the three grids and it is shown that the grid used for the simulations (55x150x55) reproduces well the prediction of the maximum of kinetic energy and it is a good compromise between accuracy and computational costs.

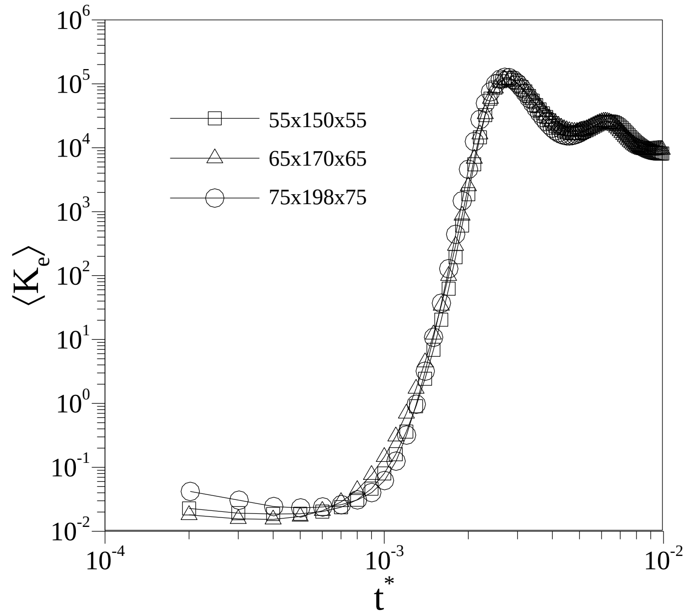

Figure 2.Time evolution of the volume averaged kinetic energy for three different grids.

3-RESULTS AND DISCUSSION

3.1. Unsteady one-dimensional pure diffusion solutions

We examined the form of the analytical solutions (see Appendix A) within the typical ranges of the diffusion coefficients [20]. Specifically,

$$-1.3 \le D_{12}^*,\ D_{21}^* \le 1.3,\ 0.5 \le D_{22}^* \le 2.5, \tag{10}$$

Solutions can be classified into four types [31]. Figure 3 shows examples of these four types of solutions for the initial mass fractions expressed in Equation 9. In Figure 3 the vertical axis corresponds to the non-dimensional vertical direction (defined as $\eta = y^*/2\sqrt{t^*}$) in which the gravity acts ($\vec{g} = -g\,\vec{j}$). The density profiles included in this figure are computed using Equation 1.

Figure 3a shows a density profile corresponding to a stable stratification (Type I solution) along the vertical direction (i.e. $\partial\rho/\partial\eta \leq 0$ in the range $\eta \in (-\infty, \infty)$). Figure 3b exhibits two symmetrically distributed unstable zones of the density profile with respect to $\eta = 0$ (Type II solution) satisfying $\partial\rho/\partial\eta > 0$ for $\eta > 1.0$ and $\eta < -1.0$. The density profile in Figure 3c shows a single unstable zone centered at $\eta = 0$ (Type III solution) combining the condition $\partial\rho/\partial\eta > 0$ in the range $-0.2 < \eta < 0.2$ together with $(\partial^2\rho/\partial\eta^2)/\eta > 0$ in the range $\eta \, \epsilon \, (-0.4, 0.4)$. Finally Figure 3d corresponds to a stable density stratification but with an unstable central region $\eta \, \epsilon \, (-0.9, 0.9)$ in which $(\partial^2\rho/\partial\eta^2)/\eta > 0$ (Type IV solution). Mention that the instability condition $(\partial^2\rho/\partial\eta^2)/\eta > 0$ does not require the appearance of density inversions, it is enough the presence of extra inflexion points on the density profile [27, 30, 31].

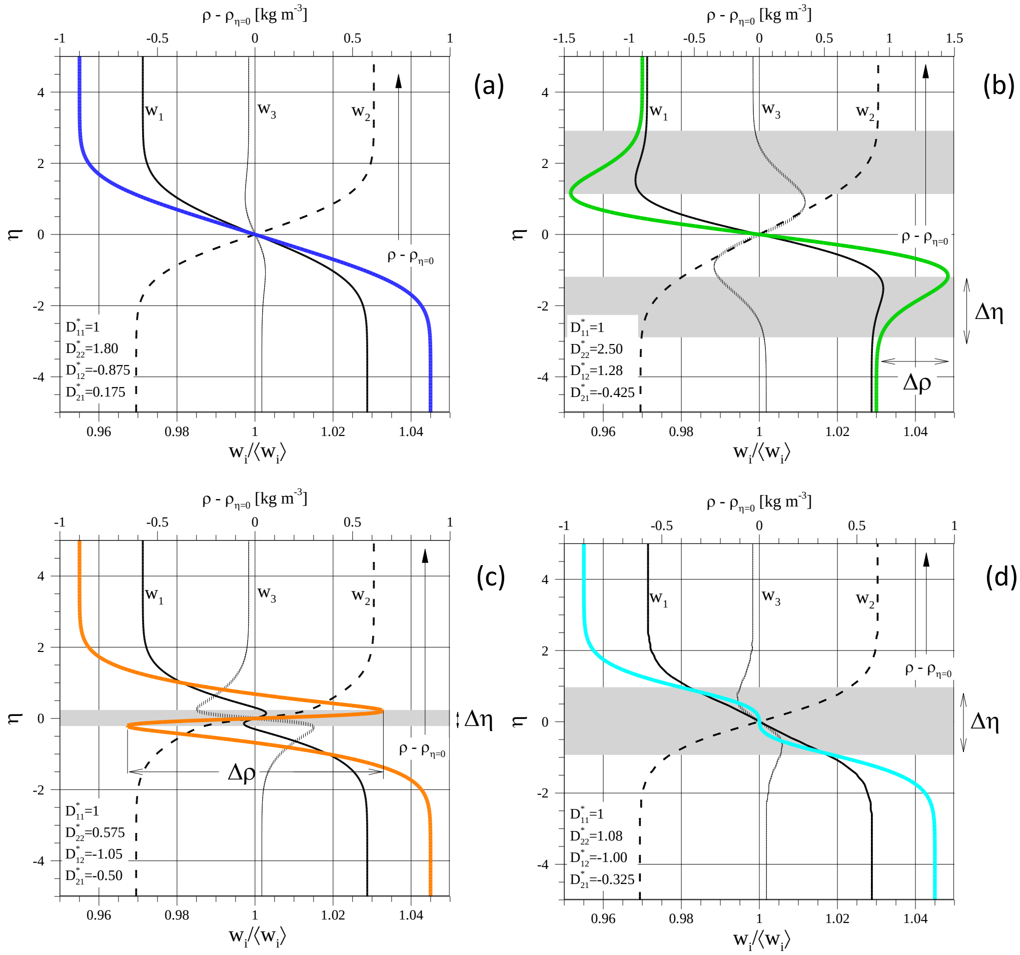

Figure 3. Examples of concentration and density vertical profiles. (a) Type I. Stable solution. (b) Type II. Two symmetrically distributed unstable zones, with respect to $\eta = 0$, indicated in grey. (c) Type III. An unstable zone, indicated in grey, centered at $\eta = 0$. (d) Type IV. An unstable zone indicated in grey, centered at $\eta = 0$. The corresponding sets of non-dimensional values of diffusion coefficients are included in each graph.

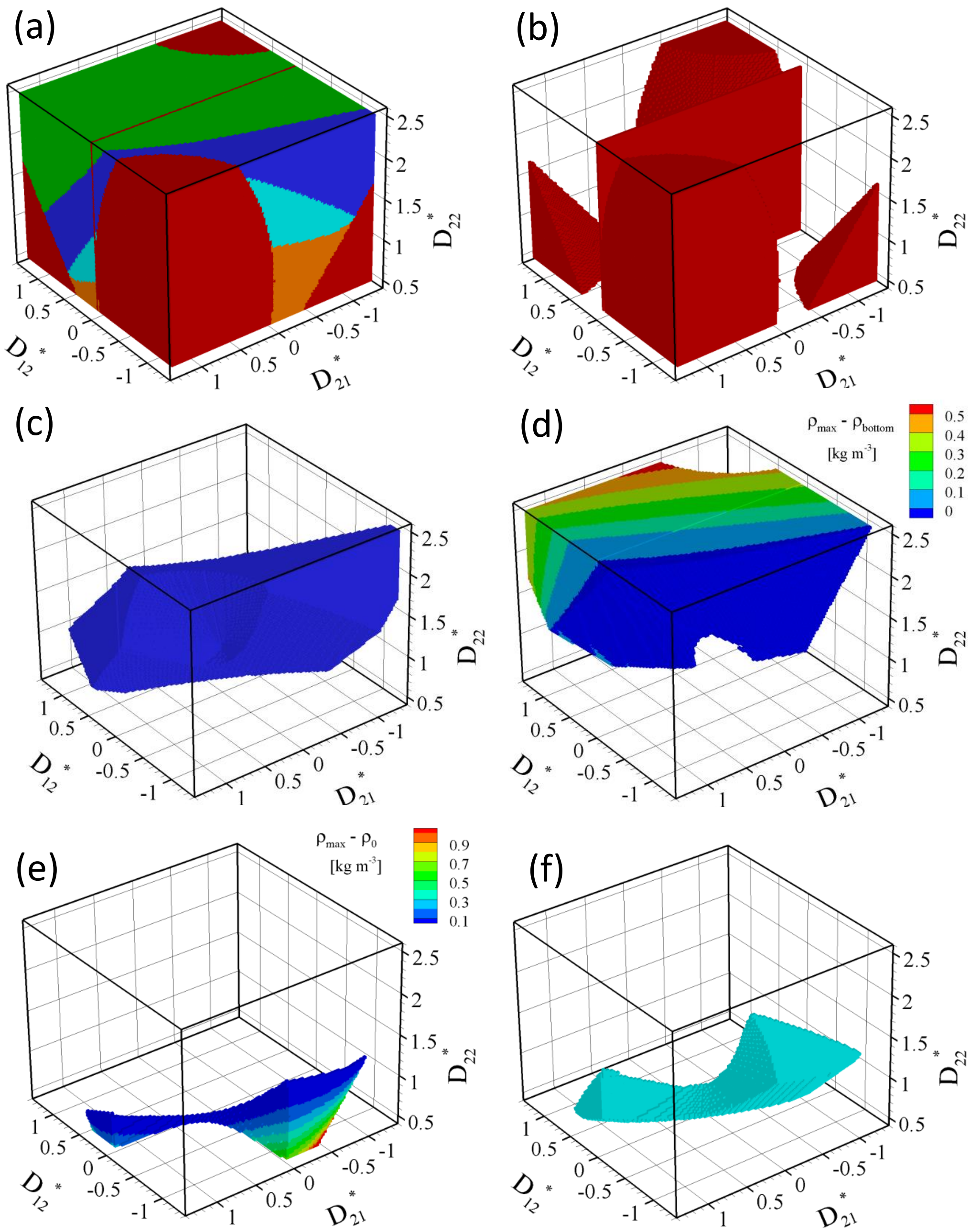

Figure 4. (a) Phase diagram of the different types of solutions. Red: Region of non-physical solutions. Dark blue: Type I. Green: Type II. Orange: Type III. Light blue: Type IV. (b) Region of non-physical solutions. (c) Type I. (d) Type II. The color indicates the difference between the maximum density and the density at $\eta \to -\infty$ (e) Type III. The color indicates the difference between the local maximum density and the density at $\eta = 0$ (f) Type IV.

Figure 4a depicts the stability map of each type of solution in the ranges of diffusion coefficients indicated in Equation 10 for the initial conditions given by Equation 9. In this figure, Type I solutions are plotted in dark blue, Type II in green, Type III in orange and Type IV in light blue. The red zones correspond to combinations of diffusion coefficients that lead to non-physical solutions to Equations 2 and 3. These combinations do not satisfy at least one of the restrictions expressed in Equation 4. The individually colored regions of Figure 4a are shown in Figures 4b to 4e. The region corresponding to the solutions of Type II (Fig. 4d) has been colored with the difference between the maximum density and the density at $\eta \to -\infty$ (see Fig.3b). Similarly, the color of the region of solutions of Type III shown in Figure 4e indicates the density difference between the value at the local maximum and the local minimum (see Figure 3c).

It can be seen that most of the physical solutions belongs to Type I (Fig. 4c) and Type II (Fig. 4d) and that the relative maximum density differences in the unstable regions of the Type II profiles are about $\Delta\rho/\rho_0 = 6 \cdot 10^{-4}$ for the example considered. Type III solutions (Fig. 4e) are less probable but can generate relative maximum density differences of about $\Delta\rho/\rho_0 = 1.2 \cdot 10^{-3}$ in relatively thin regions centered at $\eta = 0$ (see Fig.3c).

Table 1 summarizes the frequency of each type of solution in the ranges of diffusion coefficients indicated in Equation 10 for different initial conditions used in real diffusion experiments. This frequency can be associated with the volume of each type of solution in the three-dimensional stability map (as that shown in Fig. 4) with respect to the total volume occupied by the four types of solutions. It can be seen that solutions of Types III and IV are less frequent that those of Type I and Type II and that, in general, these frequencies considerably diminishes as the initial density difference between the mixtures at the bottom and the top parts of the cell is larger than 2 kg/m^3. Also, for initial density differences larger than this value Table 1 shows that the Type I and Type II solutions have frequencies between 40%-80% and 30%-20%, respectively.

	Mialdun et al. [13]				Larrañaga et al. [20]	
	Exp #1	Exp #2	Exp #3	Exp #4	Exp #1	Exp. #2
w_{in1}^{top}	0.31996	0.34006	0.31998	0.31982	0.3033	0.3033
w_{in1}^{bot}	0.33891	0.33994	0.34002	0.33962	0.3633	0.3633
w_{in2}^{top}	0.34001	0.31997	0.33998	0.32003	0.3433	0.3333
w_{in2}^{bot}	0.31991	0.34006	0.34007	0.33953	0.3233	0.3333
$\rho^{top\,(1)}$	841.4	845.7	841.4	843.7	838.2	837.0
$\rho^{bot\,(1)}$	845.7	843.5	843.5	843.5	848.9	850.1
$\rho^{bot} - \rho^{top\,(1)}$	1.8	2.3	4.4	6.6	10.7	13.0
% Type I	28	38	76	73	65	76
% Type II	59	28	23	24	33	23
% Type III	5	8	0.002	0.04	0.008	0.02
% Type IV	8	26	1	3	2	1

Table 1. Frequency of the different types of solutions for different initial mass fractions.$^{(1)}$[kg m^{-3}]

3.2. Linear stability analysis and numerical simulations of the unsteady solutal convection

To determine if the zones with unstable density stratification of Type II and Type III can induce convective motions we applied a linear stability analysis to the convection governing equations. Additionally full three-dimensional numerical simulations were carried out to predict the occurrence, the topology and the intensity of the convection flows for Types II, III and IV.

Table 2 summarizes the conditions of the simulations. The initial mass fractions considered are those of Exp#1 reported by [13] indicated in Table 1. The highest pair of Rayleigh numbers (Ra_1, Ra_2) corresponds to a cell dimension of 5 mm and to the gravity acceleration on the Earth.

<table>
<tr><th>L
[m]</th><th>g
[m s^{-2}]</th><th>μ
[Pa·s]</th><th>D_{11}
[m^2 s^{-1}]</th><th>Type</th><th>D_{22}^*</th><th>D_{12}^*</th><th>D_{21}^*</th><th>Ra_1</th><th>Ra_2</th><th>Sc</th></tr>
<tr><td>$5\cdot10^{-3}$</td><td>9.81</td><td rowspan="12">$1.29\cdot10^{-3}$</td><td rowspan="12">$1.61\cdot10^{-9}$</td><td rowspan="4">II</td><td rowspan="4">2.50</td><td rowspan="4">1.28</td><td rowspan="4">-0.425</td><td>$1.78\cdot10^{8}$</td><td>$9.47\cdot10^{7}$</td><td rowspan="12">$1.32\cdot10^{3}$</td></tr>
<tr><td colspan="2" rowspan="3"></td><td>$3.56\cdot10^{7}$</td><td>$1.89\cdot10^{7}$</td></tr>
<tr><td>$1.78\cdot10^{7}$</td><td>$9.47\cdot10^{6}$</td></tr>
<tr><td>$1.78\cdot10^{6}$</td><td>$9.47\cdot10^{5}$</td></tr>
<tr><td>$5\cdot10^{-3}$</td><td>9.81</td><td rowspan="4">III</td><td rowspan="4">0.575</td><td rowspan="4">-1.05</td><td rowspan="4">-0.50</td><td>$1.78\cdot10^{8}$</td><td>$9.47\cdot10^{7}$</td></tr>
<tr><td colspan="2" rowspan="3"></td><td>$3.56\cdot10^{7}$</td><td>$1.89\cdot10^{7}$</td></tr>
<tr><td>$1.78\cdot10^{7}$</td><td>$9.47\cdot10^{6}$</td></tr>
<tr><td>$1.78\cdot10^{6}$</td><td>$9.47\cdot10^{5}$</td></tr>
<tr><td>$5\cdot10^{-3}$</td><td>9.81</td><td rowspan="4">IV</td><td rowspan="4">1.08</td><td rowspan="4">-1.00</td><td rowspan="4">-0.325</td><td>$1.78\cdot10^{8}$</td><td>$9.47\cdot10^{7}$</td></tr>
<tr><td colspan="2" rowspan="3"></td><td>$3.56\cdot10^{7}$</td><td>$3.56\cdot10^{7}$</td></tr>
<tr><td>$1.78\cdot10^{7}$</td><td>$1.78\cdot10^{7}$</td></tr>
<tr><td>$1.78\cdot10^{6}$</td><td>$1.78\cdot10^{6}$</td></tr>
</table>

Table 2. Conditions of the simulations.

The analytical solutions to the unsteady one-dimensional diffusion process indicate that the thickness of the unstable layers grow as

$$\delta^*(t^*) = 2\Delta\eta\sqrt{t^*} \tag{11}$$

For Type II solutions $\Delta\eta \approx 2$, (see Fig. 3b) and the layers grow as $\delta^*(t^*) \approx 4\sqrt{t^*}$. For Type III solutions $\Delta\eta \approx 0.4$, (see Fig. 3c) and the layer grows as $\delta^*(t^*) \approx 0.8\sqrt{t^*}$ and for Type IV, $\Delta\eta \approx 1.8$, (see Fig. 3d) and the layer grows as $\delta^*(t^*) \approx 3.6\sqrt{t^*}$

According to the linear stability analysis (details are included in Appendix B) the convective motions appear when the thickness of the unstable stratification layer reaches the value given by Equation 12

$$\delta_c^* = \frac{3\pi^{4/3}}{2^{2/3}}\Re\left[\left(\frac{D_{12}^*D_{21}^* - D_{22}^*}{[Ra_1(D_{12}^*\Delta w_{2b} - D_{22}^*\Delta w_{1b}) + Ra_2(D_{21}^*\Delta w_{1b} - \Delta w_{2b})]}\right)^{1/3}\right] \tag{12}$$

The horizontal wavelength of the perturbations is

$$\lambda_c^* = \frac{\lambda_c}{\delta_c} = \frac{2\pi}{a_c} \approx 2.828 \tag{13}$$

which is the same that the classical result for the stress-free Rayleigh-Bénard convection (see for example [41]). Table 3 shows the prediction of the minimum thickness for the different cases considered in the simulations. The values of Δw_{1b} and Δw_{2b}, which are the increments of mass fractions between the top and the bottom of the unstable layer, are calculated using the analytical solution of the unsteady pure diffusion situation (Eqs. A-8 and A-9).

Type	D_{22}^{*}	D_{12}^{*}	D_{21}^{*}	Δw_{1b}	Δw_{2b}	Ra_1	Ra_2	δ_c^{*}	t_c^{*}
II	2.50	1.28	-0.425	$5.86\cdot10^{-4}$	$3.67\cdot10^{-3}$	$1.78\cdot10^{8}$	$9.47\cdot10^{7}$	0.1071	0.0007
						$3.56\cdot10^{7}$	$1.89\cdot10^{7}$	0.1832	0.0021
						$1.78\cdot10^{7}$	$9.47\cdot10^{6}$	0.2308	0.0033
						$1.78\cdot10^{6}$	$9.47\cdot10^{5}$	0.4973	0.0155
III	0.575	-1.05	-0.50	$1.52\cdot10^{-3}$	$8.50\cdot10^{-3}$	$1.78\cdot10^{8}$	$9.47\cdot10^{7}$	0.0232	0.0008
						$3.56\cdot10^{7}$	$1.89\cdot10^{7}$	0.0397	0.0025
						$1.78\cdot10^{7}$	$9.47\cdot10^{6}$	0.0500	0.0039
						$1.78\cdot10^{6}$	$9.47\cdot10^{5}$	0.1078	0.0182
IV	1.08	-1.00	-0.325	-0.010	0.0150	$1.78\cdot10^{8}$	$9.47\cdot10^{7}$	0.0644	0.0003
						$3.56\cdot10^{7}$	$1.89\cdot10^{7}$	0.1101	0.0009
						$1.78\cdot10^{7}$	$9.47\cdot10^{6}$	0.1387	0.0015
						$1.78\cdot10^{6}$	$9.47\cdot10^{5}$	0.2988	0.0069

Table 3.Critical thicknesses of the unstable layers and the corresponding critical times.

It can be seen that, for a given pair of Rayleigh numbers, the critical thickness for Type II and Type IV solutions is about 4.6 times larger than for Type III solutions. However the unstable layers for Type III solutions grow 5 times faster than for Type II. This produces similar critical times for Type II and Type III solutions, as shown in Table 3.

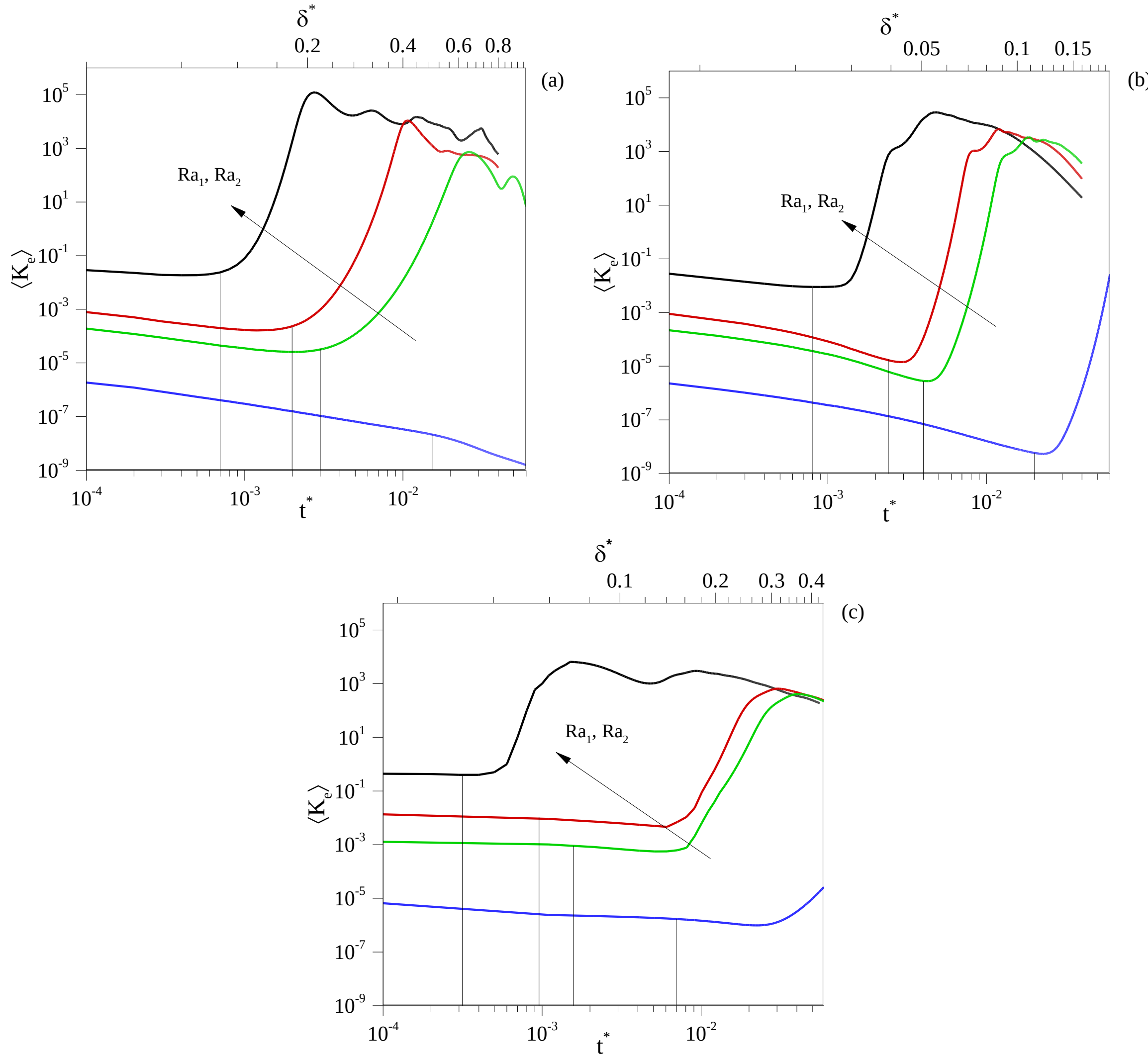

Figure 5. Time evolution of the volume averaged kinetic energy for simulations of (a) Type II, (b) Type III and (c) Type IV. The corresponding Rayleigh numbers are indicated in Table 2. The scales at the top horizontal axes correspond to the time evolution of the thickness of the unstable layers for the pure diffusion conditions.

Figure 5 shows the time evolutions of the volume averaged kinetic energy predicted by the numerical simulations carried out with the parameters indicated in Table 2. Note that the vertical scale of the plots is logarithmic and that under the physical conditions considered, a value of the non-dimensional kinetic energy of 0.1 corresponds to a fluid velocity of about 0.1μm/s (i.e. 0.36 mm/h), which can be considered negligibly small. As a reference of time, the pure diffusion process reaches the horizontal walls of the cell (i.e. changes in the density larger than 1% in comparison with the initial values) at non-dimensional times of 0.02 for Type II and Type III solutions. Figure 5 shows that convective motions are initiated, in general, well before this time for the three largest pair of Rayleigh numbers considered in the simulations. It can be seen that the initiation of the increase of the kinetic energy is delayed in time as the Rayleigh number decreases. The critical times obtained with the linear stability analysis shown in Table 3 are indicated in Figure 5 along the bottom horizontal axes. It can be seen that they agree with the time, predicted by the simulations, at which the kinetic energy starts to increase for solutions of Type II and Type III that exhibit fluid layers with density inversions (see Fig. 3b and 3c). In the case of Type IV solutions, in which the instability is produced by the condition $(\partial^2\rho/\partial\eta^2)/\eta > 0$ (see Fig. 3d), the linear stability analysis underpredict the time for the onset of convection, especially at low Rayleigh numbers. This is produced probably because in this case the rate of growth of the perturbations is comparable to the rate of change of the concentrations corresponding to the quiescent state (i.e. $\partial w_i'/\partial t \approx \partial w_{ib}/\partial t$, see Appendix B) and the quasi-steady state assumption for the evolution of the concentrations, used to obtain Eq. 12, is not completely satisfied. Figure 5a, corresponding to the Type II solutions, shows that for the lowest pair of Rayleigh numbers the simulation does not predict the increase of kinetic energy after the critical time obtained with the linear stability analysis ($t_c^* = 0.0155$). At this time, the thickness of the unstable layers is about $\delta^* \approx 0.5$ (see Table 3) and the centers of the pair of unstable layers, located near $\eta \approx \pm 2$ (see Fig. 3a), are at a distance of the horizontal walls of about $0.5L$. This relatively large thickness of the unstable layer, in comparison with the cell dimensions, avoids the growth of perturbations with the critical wavelength obtained with the linear stability analysis ($\lambda_c = 2.828$). Note that this wavelength corresponds to a layer with an aspect ratio (width/height) of $0.35L$ and that for an unstable layer with this thickness the stabilizing effect of the solid lateral walls of the cell damps the growth of the perturbations.

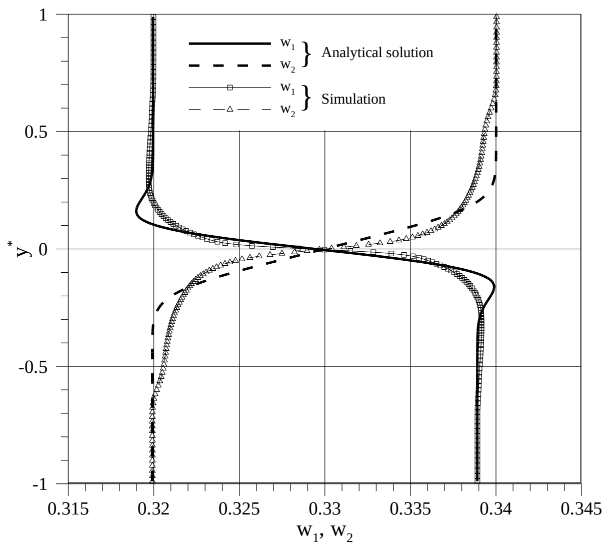

Figure 6. Mass fraction profiles at $t^* = 2.8 \cdot 10^{-3}$ for Type II solutions at $Ra_1 = 1.78 \cdot 10^8$ and $Ra_2 = 9.47 \cdot 10^7$

As an example of the deviations of the pure diffusion situation that the convective motions generated in the unstable layers can produce, Figure 6 shows the vertical profiles of the mass fractions at $t^* = 2.8 \cdot 10^{-3}$ for Type II solutions at the largest pair of Rayleigh numbers. As shown in Figure 5a, at this time, the maximum of the kinetic energy occurs. The profiles corresponding to the numerical simulation have been obtained by averaging the values of the mass fractions on each horizontal plane. It can be seen that differences between the theoretical pure diffusion situation and the *actual* convective situation are important and that the convection flows tend to smooth the concentration profiles due to mixing. At this specific time, the set of diffusion coefficients in the analytical solutions that best fits the density profile corresponding to the numerically simulated mass fractions in Figure 6 is $D_{22}^* = 0.50$, $D_{12}^* = 0.875$, $D_{21}^* = 0.50$. These values are very different of the set used in the simulations (see Table 3).

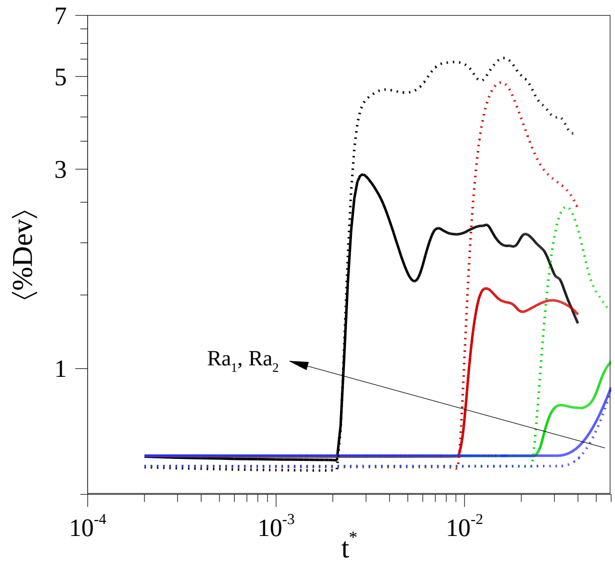

Figure 7.Time evolution of the deviation with respect to the pure diffusion situation for Type II solutions. Continuous lines:w_1. Dashed lines: w_2

Figure 7 shows, for the Type II solution, the time-evolution of the average deviation of the mass fraction profiles numerically predicted with respect to the analytical solution. A similar plot is obtained for the Type III solution and it has been omitted here for sake of brevity. The deviation of the numerical profile for each component of the mixture is defined as,

$$\langle \%Dev_i \rangle = 100 \, \langle \frac{\left|(w_i(y))_{analytical} - \overline{(w_\iota)(y)}_{simulation}\right|}{(w_i)_{ini}^{top} - (w_i)_{ini}^{bot}} \rangle \qquad (14)$$

It can be seen in Figure 7 that for the three largest pairs of Rayleigh numbers, at which intense convective motions occur (see Fig. 6a), maximum deviations range between 2% and 7%. As a reference the profiles of component 1 and component 2 shown in Figure 6 have deviations of 4.2% and 2.9%, respectively. For the lowest pair of Rayleigh numbers, at which simulations predict a pure diffusion situation (see Fig. 6a), deviations start to be evident for $t^* > 0.05$, this is well after the diffusion process has reached the horizontal walls of the cell and the validity of the analytical solution for an infinite one-dimensional domain fails.

To illustrate the flow structures generated by the convective motions Figures 8.II-a, 8.III-a and 8.IV-a show isosurfaces of the vertical velocity component and Figures 8.II-b, 8.III-b and 8.IV-b contours of the mass fractions of component 1 superimposed to the velocity vector field along a vertical diagonal plane. Animations of the flow structures are available as Supplementary material and descriptions are included in Appendix C.

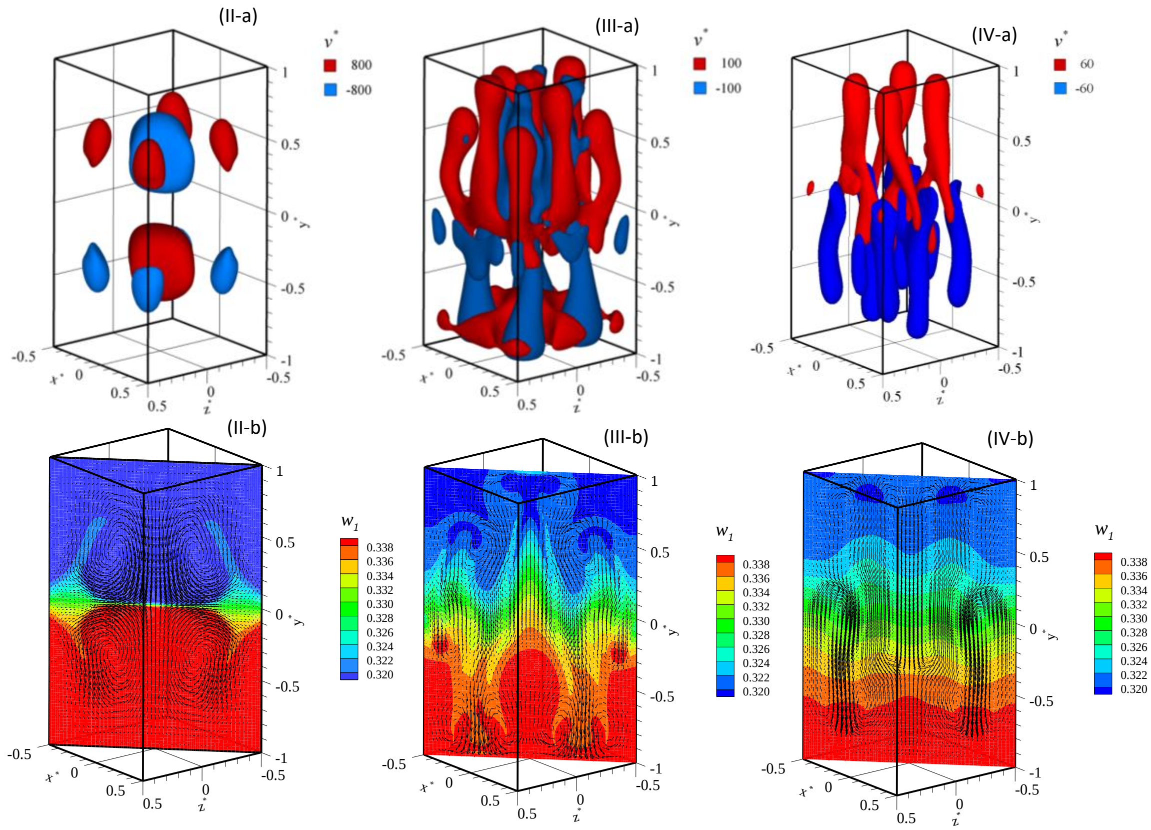

Figure 8. Snapshots of the instantaneous flow structures for solutions of Type II ($Ra_1 = 1.78 \cdot 10^8, Ra_2 = 9.47 \cdot 10^7, t^* = 2.8 \cdot 10^{-3}$), Type III ($Ra_1 = 3.56 \cdot 10^7, Ra_2 = 1.89 \cdot 10^7, t^* = 1.23 \cdot 10^{-2}$) and Type IV ($Ra_1 = 3.56 \cdot 10^7, Ra_2 = 1.89 \cdot 10^7, t^* = 2.00 \cdot 10^{-2}$). II.a, III.a and IV.a: Isosurfaces of the vertical velocity component for Type II, Type III and Type IV solutions, respectively. II.b, III.b and IV.b: Contours of mass fraction of component 1 and velocity vectors on a vertical diagonal plane.

It can be seen in Figures 8.II-a and 8.II-b that the flow is antisymmetric with respect to the horizontal midplane of the cell ($y^* = 0$). In the top/bottom half of the cell the flow ascends/descends near the four vertical edges and descends/ascends along the vertical axis of the cell. This flow structure can be understood as two toroidal rolls; one toroidal roll in each half of the diffusion cell. The toroidal rolls have been observed numerically and experimentally in Rayleigh-Bénard flows in cubical cavities [35, 42]. Figure 8II-b shows that the combined effect of the two toroidal rolls on the mass fraction distribution is the increase of the thickness of the mixing layer near the sidewalls of the cell and the decrease of this thickness in the center.

Figures 8.III and 8.IV show that for the Type III and Type IV solutions the flow consists in arrays of relatively thin, ascending and descending plumes that produce intense mixing. It can be seen comparing the vector fields of Figures 8.II-b and 8.III-b that the rolling motions of both figures have different horizontal wavelength. The flow shown in Figure 8.II-b has two rolling motions along the horizontal direction (i.e. the wavelength is the distance between two diagonally opposed vertical edges).In the case of the flow shown in Figure 8.III-b (Type III solution) or Figure 8.IV-b (Type IV solution) the horizontal wavelength of the rolling motions is about a half of that in Figure 8.II-b (Type II solution). Note that, according to the linear stability analysis, perturbations in the Type II solution grow initially in a layer of thickness $\delta_c^* \approx 0.1$ (see Table 3) while perturbations the Type III solution grow in an unstable layer of thickness $\delta_c^* \approx 0.04$ (i.e. about a half of that in the Type II solution). This reduced thickness allows the growth of perturbations with a smaller wavelength, that evolve into the relatively thin plumes shown in Figure 8.III-a.

4-CONCLUSIONS

We analyzed the unsteady diffusion process of ternary mixtures under the conditions of experiments carried out to determine the diffusion coefficients. In these situations it is known that cross diffusion terms generate four types of solutions to the one-dimensional unsteady diffusion equations in ternary mixtures, depending on the specific set of diffusion coefficients and initial conditions. In the case of a diffusion process initiated with a stable stratification (i.e. the denser mixture at the bottom and the lighter at the top), two types of solutions (Type II and Type III) generate fluid layers with unstable density stratification. In the other two types of solutions (Type I and Type IV) the stratification is stable but one type (Type IV) has an unstable fluid layer associated with the sign of the second derivative of density with respect to the vertical direction. Within the usual ranges of diffusion coefficients Type I and Type II solutions have frequencies between 40%-80% and 30%-20%, respectively, depending on the initial concentrations of the components of the mixture. Type III solutions are less frequent with maximum frequencies of about 8%. The occurrence of Type IV solutions ranges between 26% and 1% with a strong dependence on the initial conditions.

To illustrate the convection flows that can be generated, full three-dimensional numerical simulations have been conducted of the unsteady diffusion processes in a ternary mixture under the conditions of experiments carried out in a diffusion cell. For the simulations we considered different sets of diffusion coefficients corresponding to the Type II, Type III and Type IV solutions and different Rayleigh numbers. The linear stability analysis indicates a minimum thickness of the unstable layers with density inversions (Type II and Type III) for the onset of convection which is in agreement with the simulations and predicts the same critical wavelength of the perturbations as in the classical Rayleigh-Bénard flow with stress free boundary conditions. In the case of Type IV solutions the linear stability analysis underpredicts the time at which the onset of convection is observed in the numerical simulations, especially at low Rayleigh numbers. The onset of convection in Type II solutions, that generate two unstable layers, is numerically observed at about the same times as in Type III solutions, which has a single unstable layer. However the different rates of growth of the unstable layers ($\delta^*(t^*) \approx 4\sqrt{t^*}$, for Type II solutions and$\delta^*(t^*) \approx 0.8\sqrt{t^*}$ for Type III solutions) produce that the onset of convection occurs at larger layer thicknesses for Type II solutions than for Type III solutions.

For the sets of Rayleigh numbers and diffusion coefficients considered, large-scale convective motions are generated for Type II, Type III and Type IV solutions, which produce significant departures of the concentration distributions from the pure diffusion situation. The instability in Type III and Type IV solutions is initiated in relatively thin layers and a flow pattern consisting in arrays of ascending and descending plumes is observed. For Type II solutions antisymmetric large-scale toroidal shaped flows develop in the two halves of the diffusion cell.

Acknowledgements

The authors specially thank Dr. M. Bou-Ali (Mondragon Unibertsitatea) for his expert advice in the first steps of the work. This study has been supported by the Spanish Ministerio de Economía y Competitividad (MINECO) under projects CTQ2013-46799-C2-1-P, granted to JP, and ESP2014-53603-P, to and JG and XR.

REFERENCES

[1] Platten, J.K. (2006) The Soret Effect: A Review of Recent Experimental Results, *Journal of Applied Mechanics* **73**, 5-15.

[2] Martin A., Bou-Ali M., Barrutia H., Alonso de Mezquia D. (2011) Microfluidic separation process by the Soret effect in biological fluids*, Comptes Rendus Mecanique* **339**, 342-348.

[3] Srinivasan S., Saghir M.Z. (2011)Experimental approaches to study thermodiffusion – A Review*, International Journal of Thermal Sciences* **50**, 1125-1137.

[4] Rahman M.A., Saghir M.Z. (2014) Thermodiffusion or Soret effect: Historical review, *International Journal of Heat and Mass Transfer* **73**, 693-705.

[5] VanVaerenberg S.,Legros J.C., Daridon J.L., Karapantsios T., Kostoglou M. Saghir M.Z. (2006) Multicomponent transport studies of crude oils and asphaltenes in DSC program, *Microgravity Science and Technology* XVIII-3/4, 150-154.

[6] Touzet M., Galliero G., Lazzeri V., Saghir M.Z., Montel F., Legros J.C. (2011) Thermodiffusion: From microgravity experiments to the initial state of petroleum reservoirs*, Comptes Rendus Mecanique* **339**, 318-323.

[7] Urteaga P., Bou-Ali M., Alonso de Mezquia D., Santamaria J., Santamaria C., Madariaga J.A., Bataller H. (2012) Measurement of thermodiffusion coefficient of hydrocarbon binary mixtures under pressure with the thermogravitational technique, *Review of Scientific Instruments* **83**, 074903.

[8] VanVaerenberg S., Srinivasan S., Saghir M.Z. (2009*)* Thermodiffusion in multicomponent hydrocarbon mixtures: Experimental investigations and computational analysis, *The Journal of Chemical Physics* **131**, 114505.

[9] Sechenyh V., Legros J.C., Mialdun A., Ortiz de Zárate J.M., Shevtsova V. (2016) Fickian diffusion in ternary mixtures composed by 1,2,3,4-Tethahydronaphtalene, Isobutylbenzene and n-Dodecane, The Journal of Physical Chemistry B **120,** 535-548.

[10] Ahadi A., Saghir M.Z. (2015) Contribution to the benchmark for ternary mixtures: Transient analysis in microgravity conditions, *The European Physical Journal E,* 38:25.

[11] Ahadi A., Saghir M.Z. (2016) The microgravity DSC-DCMIX1 mission onboard ISS: Experiment description and results on the measurement of the Soret coefficients for isobutylbenzene, dodecane, tetralin ternary hydrocarbons mixtures, *Experimental Thermal and Fluid Science* **74**, 296-307.

[12] Mialdun, A., Sechenyh, V., Legros, J. C., Ortiz de Zárate, J.M., Shevtsova, V. (2013a) Investigation of Fickian diffusion in the ternary mixture of 1, 2, 3, 4-tetrahydronaphthalene, isobutylbenzene, and dodecane, *The Journal of Chemical Physics* **139,** 104903.

[13] Mialdun A., Yasnou V., Shevtsova V. (2013b) Measurement of isothermal diffusion coefficients in ternary mixtures using counter flow diffusion cell, *Comptes Rendus, Mecanique* **341**, 462 – 468.

[14] Mialdun A., Shevtsova V. (2008) Development of optical digital interferometry technique for measuremenmt of thermodiffusion coefficients, *International Journal of Heat and Mass Transfer* **51**, 3164-3178.

[15] Mialdun A., Shevtsova V. (2011) Digital interferometry as a powerful tool to study the thermodiffusion effect, *Comptes Rendus Mecanique* **339**, 362-368.

[16] Shevtsova V., Sechenyh V., Nepomnyashchy, Legros J.C. (2011) Analysis of the application of optical two-wavelength techniques to measurement of the Soret coefficients in ternary mixtures, *Phylosophical Magazine* **91**, 3498-3518.

[17] Blanco P., Bou-Ali M. M., Platten J. K., de Mezquia D. A., Madariaga J. A., Santamaria C. (2010) Thermodiffusion coefficients of binary and ternary hydrocarbon mixtures, *The Journal of Chemical Physics* **132**, 114506.

[18] Alonso de Mezquia D., Bou-Ali M., Larrañaga M., Madariaga J.A., Santamaria, C. (2012) Determination of Molecular Diffusion Coefficients in n-Alkane Binary Mixtures: Empirical correlations, *The Journal of Physical Chemistry B* **116**, 2814-2819.

[19] Larrañaga M., Bou-Ali M. M., Soler D., Martinez-Aguirre M., Mialdun A., Shevtsova V. (2013) Remarks on the analysis methods for determining diffusion coefficients in ternary mixtures, *Comptes Rendus Mecanique* **341**, 356 – 364.

[20] Larrañaga, M., Rees, D.A.S., Bou-Ali, M. M. (2014) Determination of the molecular diffusion coefficients in ternary mixtures by the sliding symmetric tubes technique, *The Journal of Chemical Physics* **140**, 054201.

[21] Larrañaga, M., Bou-Ali, M. M., de Mezquía, D. A., Rees, D. A. S., Madariaga, J. A., Santamaría, C., Platten, J. K. (2015). Contribution to the benchmark for ternary mixtures: Determination of Soret coefficients by the thermogravitational and the sliding symmetric tubes techniques, *The European Physical Journal E*, *38:28*.

[22] Leahy-Dios A., Bou-Ali M. M., Platten J.K., Firozabadi A. (2005)Measurements of molecular and thermal diffusion coefficients in ternary mixtures, *The Journal of Chemical Physics* **122**, 234502.

[23] Galand Q., Van Vaerenberg S. (2015) Contribution to the benchmark for ternary mixtures: Measurement of diffusion and Soret coefficients of ternary system tetrahydropnaphtalene-isobutiylbenzene-n-dodecane with mass fractions 80-10-10 at 25°C, *The European Physical Journal E,* 38:26.

[24] Sechenyh V., Legros J.C., Shevtsova V. (2013) Development and validation of a new setup for measurements of diffusion coefficients in ternary mixtures using the Taylor dispersion technique, *Comptes Rendus Mecanique* **341**, 490-496.

[25] Gebhardt M., Khöler W. (2015) What can be learned from optical two-color diffusion and thermodiffusion experiments on ternary fluid mixtures, *The Journal of Chemical Physics* **142**, 084506.

[26] Khlybov O.A., Ryzhov I., Lyubimova T. (2015) Contribution to the benchmark for ternary mixtures: Measurement of diffusion and Soret coefficients in 1,2,3,4-tetrahydronaphtalene, isobutylbenzene and dodecane onboard the ISS, *The European Physical Journal E*, *38:29.*

[27] Vitagliano P.L., Ambrosone L., Vitagliano V. (1992) Gravitational instabilities in multicomponent free-diffusion boundaries, *The Journal of Physical Chemistry* **96,** 1431-1437.

[28] Ambrosone L. (2000) Double-diffusive instability in free diffusing layers: A general formulation, *Physica B* **292,** 136-152.

[29] Vitagliano P.L., Andreozzi M., Catagnolo D., Vitagliano V. (2001) Experimental test and numerical simulation of double diffusive convection in isothermal three component diffusion boundaries, *Journal of Molecular Liquid*s **94**, 113-126.

[30] Budroni M.A. (2015) Cross-diffusion-driven hydrodynamic instabilities in a double-layer system: General classification and nonlinear simulations, *Physical Review E* **92**, 063007.

[31] Miller D. G., Vitagliano V. (1986) Experimental test of McDougall's theory for the onset of convective instabilities in isothermal ternary systems, *The Journal of Physical Chemistry*, **90**(8), 1706-1717.

[32] Vitagliano V., Catagnolo D., De Chiara G., Vitaglaino P.L., De Luca D., Pannico M., Tommasone M., Villani M., Zampino P. (2003) Diffusion boundaries behaviour during a parabolic flight, *Microgravity Science and Technology* **XIV**/4, 21-26.

[33] Budroni M.A., Carballido-Landeira J., Intiso A., De Wit A., Rossi F. (2015) Interfacial hydrodynamic instabilities driven by cross-diffusion in reverse microemulsions, *Chaos* **25**, 064502.

[34] Taylor R., Krishna R., *Multicomponent Mass Transfer*, Wiley (New York) 1993.

[35] Pallares, J., Grau, F. X., Giralt, F. (1999) Flow transitions in laminar Rayleigh–Bénard convection in a cubical cavity at moderate Rayleigh numbers, *International Journal of Heat and Mass Transfer* **42**, 753-769.

[36] Pallares, J., Vernet, A., Ferre, J. A., Grau, F. X. (2010) Turbulent large-scale structures in natural convection vertical channel flow, *International Journal of Heat and Mass Transfer* **53**, 4168-4175.

[37] Ruiz X., Pallares J. and Grau F. X. (2010) On the accuracy of the interdiffusion measurements at low and moderate Rayleigh numbers. A computational approach, *International Journal of Heat and Mass Transfer* **53,** 3708-3720.

[38] Ruiz X., Pallares J. (2012) On the accuracy of the diffusion coefficient measurements using different shear cell configurations at low and moderate Rayleigh numbers, *International Journal of Heat and Mass Transfer* **55,** 6966-6978.

[39] Ruiz X., Saez N., Gavaldà J., Pallares J. (2015) The impact of free surfaces on the measurement of binary diffusion coefficients using shear cells, *International Journal of Heat and Mass Transfer* **81**, 602-617.

[40] Koren B., A Robust Upwind Discretization Method for Advection, Diffusion and Source Terms, Technical Report NM-R9308, Centrum voorWiskunde en Informatica, Amsterdam, April 1993.

[41] Koschmieder, E. L. *Bénard cells and Taylor vortices*. Cambridge University Press, 1993.

[42] Pallares, J., Arroyo, M. P., Grau, F. X., Giralt, F. (2001).Experimental laminar Rayleigh-Bénard convection in a cubical cavity at moderate Rayleigh and Prandtl numbers, *Experiments in Fluids* **31**, 208-218.

APPENDIX A. Analytical solutions of the one-dimensional unsteady diffusion process

One dimensional unsteady diffusion processes in ternary mixtures can be modelled with the following partial differential equations,

$$\frac{\partial w_1}{\partial t^*} = \frac{\partial^2 w_1}{\partial y^{*2}} + D_{12}^* \frac{\partial^2 w_2}{\partial y^{*2}} \quad \text{(A-1)}$$

$$\frac{\partial w_2}{\partial t^*} = D_{22}^* \frac{\partial^2 w_2}{\partial y^{*2}} + D_{21}^* \frac{\partial^2 w_1}{\partial y^{*2}} \quad \text{(A-2)}$$

When the diffusion process occurs far from bounding walls (i.e. in an infinite domain), the partial differential governing equations (Eqs. A-1 and A-2) can be transformed using the similarity variable ξ defined as,

$$\xi = \alpha\eta = \alpha \frac{y}{2\sqrt{t\, D_{11}}} = \alpha \frac{y^*}{2\sqrt{t^*}} \quad \text{(A-3)}$$

The resulting two ordinary differential equations can be written as,

$$2\,\xi\, \frac{dw_1}{d\xi} + \alpha^2 \frac{d^2 w_1}{d\xi^2} + D_{12}^* \alpha^2 \frac{d^2 w_2}{d\xi^2} = 0 \quad \text{(A-4)}$$

$$2\,\xi\, \frac{dw_2}{d\xi} + D_{21}^* \alpha^2 \frac{d^2 w_1}{d\xi^2} + D_{22}^* \alpha^2 \frac{d^2 w_2}{d\xi^2} = 0 \quad \text{(A-5)}$$

Considering an infinite fluid column, the boundary conditions are;

$$\xi \to \infty;\, w_1 = w_{in1}^{top};\, w_2 = w_{in2}^{top} \quad \text{(A-6)}$$

and

$$\xi \to -\infty;\, w_1 = w_{in1}^{bot};\, w_2 = w_{in2}^{bot} \quad \text{(A-7)}$$

The solutions to Equations A-4 to A-7 are given in Larrañaga et al. [20] and they can be written as,

$$w_1 = A\, \mathrm{erfc}(\alpha_1\eta) + B\, \mathrm{erfc}(\alpha_2\eta) + w_{in1}^{top} \quad \text{(A-8)}$$

$$w_2 = A\, \left(\frac{1-\alpha_1^2}{D_{12}^*\, \alpha_1^2}\right) \mathrm{erfc}(\alpha_1\eta) + B\, \left(\frac{1-\alpha_2^2}{D_{12}^*\, \alpha_2^2}\right) \mathrm{erfc}(\alpha_2\eta) + w_{in2}^{top} \quad \text{(A-9)}$$

where

$$A = \frac{D_{12}^{*}\,\alpha_1^2\,\alpha_2^2\left(w_{in2}^{bot} - w_{in2}^{top}\right) - \alpha_1^2\left(w_{in1}^{bot} - w_{in1}^{top}\right)\left(1 - \alpha_2^2\right)}{2\left(\alpha_2^2 - \alpha_1^2\right)} \tag{A-10}$$

$$B = \frac{D_{12}^{*}\,\alpha_1^2\,\alpha_2^2\left(w_{in2}^{bot} - w_{in2}^{top}\right) - \alpha_2^2\left(w_{in1}^{bot} - w_{in1}^{top}\right)\left(1 - \alpha_1^2\right)}{2\left(\alpha_1^2 - \alpha_2^2\right)} \tag{A-11}$$

and

$$\alpha_1 = \sqrt{\frac{-1 - D_{22}^{*} - \sqrt{(1 + D_{22}^{*})^2 + 4(D_{12}^{*}D_{21}^{*} - D_{22}^{*})}}{2(D_{12}^{*}D_{21}^{*} - D_{22}^{*})}} \tag{A-12}$$

$$\alpha_2 = \sqrt{\frac{-1 - D_{22}^{*} + \sqrt{(1 + D_{22}^{*})^2 + 4(D_{12}^{*}D_{21}^{*} - D_{22}^{*})}}{2(D_{12}^{*}D_{21}^{*} - D_{22}^{*})}} \tag{A-13}$$

APPENDIX B. Linear stability analysis

In this appendix we include the details of the linear stability analysis applied to the governing equations to determine the required conditions for the onset of convection in the layers with unstable density stratification of solutions of Type II and Type III.

We assume that each layer, in which an unstable density occurs, can be approximated as a two-dimensional fluid layer with an instantaneous thickness δ. This is valid for large aspect ratio (width/height) layers. Gravity acts along the negative y-direction (see Fig. B.1).

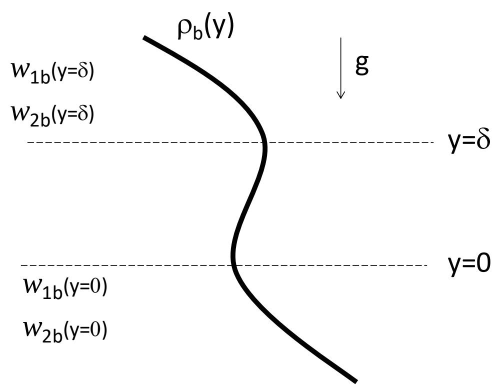

Figure B.1. Sketch of a fluid layer with unstable density stratification. The thick line indicates the vertical density profile.

The basic quiescent state in the layer, indicated with the subscript b, can be defined by the pure diffusion situation as,

$$\begin{gathered} u_{b_i} = 0;\ \frac{dp_b}{dy} = -g\ \rho_b(y);\ \rho_b = \rho_o(1 + \beta_1 w_{1b} + +\beta_2 w_{2b}) \\ \frac{\partial w_{1b}}{\partial t} = D_{11}\frac{\partial^2 w_{1b}}{\partial y^2} + D_{12}\frac{\partial^2 w_{2b}}{\partial y^2};\ \frac{\partial w_{2b}}{\partial t} = D_{21}\frac{\partial^2 w_{1b}}{\partial y^2} + D_{22}\frac{\partial^2 w_{2b}}{\partial y^2} \end{gathered} \quad \text{(B-1)}$$

According to this, the instantaneous concentrations within the layer ($w_{1b}(y)$ and $w_{2b}(y)$) are given by Equations A-8 and A-9.

The two-dimensional perturbed state is defined in Equation B-2 as the basic quiescent state plus the perturbations, which are denoted with the prime symbol.

$$u_i = u_{b_i} + u_i'; \;\; \rho = \rho_b + \rho'; \; \rho' = \rho_o(\beta_1 w_{1b}' + \beta_2 w_{2b}')$$
$$w_1 = w_{1b} + w_1'; \; w_2 = w_{2b} + w_2' \quad \text{(B-2)}$$

The streamfunction associated with the velocity perturbations is,

$$u' = \frac{\partial \psi}{\partial y}\,, v' = -\frac{\partial \psi}{\partial x} \quad \text{(B-3)}$$

We assume that the rate of growth of the perturbations is larger than the rate of change of the concentrations of the quiescent state (i.e. $\partial w_1'/\partial t \gg \partial w_{1b}/\partial t$ and $\partial w_2'/\partial t \gg \partial w_{2b}/\partial t$) and we approximate the variations of the concentrations within the layer with linear dependences (i.e. $w_{1b} = (\Delta w_{1b}/\delta)\, y + w_{1b(y=0)}$ and $w_{2b} = (\Delta w_{2b}/\delta)\, y + w_{2b(y=0)}$). According to these hypotheses, the substitution of Equations B-2 and B-3 into the governing equations and neglecting the second-order terms lead to,

$$\frac{1}{Sc}\frac{\partial}{\partial t^*}(\nabla^2 \psi^*) = \nabla^4 \psi^* + Ra_1^\delta \frac{\partial w_1'}{\partial x^*} + Ra_2^\delta \frac{\partial w_2'}{\partial x^*} \quad \text{(B-4)}$$

$$\frac{\partial w_1'}{\partial t^*} = \frac{\partial \psi^*}{\partial x^*}\Delta w_{1b} + \nabla^2 w_1' + D_{12}^* \nabla^2 w_2' \quad \text{(B-5)}$$

$$\frac{\partial w_2'}{\partial t^*} = \frac{\partial \psi^*}{\partial x^*}\Delta w_{2b} + D_{21}^* \nabla^2 w_1' + D_{22}^* \nabla^2 w_2' \quad \text{(B-6)}$$

where $Ra_1^\delta = \beta_1 g \delta^3 / \nu D_{11}$, $Ra_2^\delta = \beta_2 g \delta^3 / \nu D_{11}$ are the Rayleigh numbers based on the thickness of the unstable layer and $\Delta w_{1b} = w_{1b\,(y=\delta)} - w_{1b\,(y=0)}$ and $\Delta w_{2b} = w_{2b\,(y=\delta)} - w_{2b\,(y=0)}$ are the instantaneous increments of mass fractions between $y = \delta$ and $y = 0$, which can be computed with Eqs. A-8 and A-9. The non-dimensional variables in Equations B-4 to B-6 are obtained using δ as the length scale and δ^2/D_{11} as the time scale. The stress-free boundary conditions to Equations B-4 to B-6 are,

$$\psi^* = \nabla^2 \psi^* = w_1' = w_2' = 0 \text{ at } y^* = 0 \text{ and } y^* = 1 \quad \text{(B-7)}$$

The two-dimensional periodic perturbations are assumed to be of the form,

$$\psi^* = \Psi\, e^{\sigma t^*} sin(a x^*) sin(\pi y^*) \quad \text{(B-8)}$$

$$w_1' = \mathrm{W}_1\, e^{\sigma t^*} cos(a x^*) sin(\pi y^*) \quad \text{(B-9)}$$

$$w_2' = \mathrm{W}_2\, e^{\sigma t^*} cos(ax^*) sin(\pi y^*) \qquad \text{(B-10)}$$

where a is the wavenumber and σ is the growth rate of the perturbations.

The insertion of Equations B-8 to B-10 into Equations B-4 to B-6 and setting $\sigma = 0$, to determine the marginal stability situation, lead to,

$$\mathrm{K}^4\Psi - a\, Ra_1^\delta \mathrm{W}_1 - a\, Ra_2^\delta \mathrm{W}_2 = 0 \qquad \text{(B-11)}$$

$$-a\, \Delta w_{1b}\Psi + \mathrm{K}^2\mathrm{W}_1 + \mathrm{K}^2 D_{12}^*\mathrm{W}_2 = 0 \qquad \text{(B-12)}$$

$$-a\, \Delta w_{2b}\Psi + \mathrm{K}^2 D_{21}^*\mathrm{W}_1 + \mathrm{K}^2 D_{22}^*\mathrm{W}_2 = 0 \qquad \text{(B-13)}$$

where $\mathrm{K}^2 = (a^2 + \pi^2)$. To obtain a non-trivial solution of this linear system, we require

$$\begin{matrix} \mathrm{K}^6(D_{22}^* - D_{12}^* D_{21}^*) + \\ +a^2\left[Ra_1^\delta(D_{12}^*\Delta w_{2b} - D_{22}^*\Delta w_{1b}) + Ra_2^\delta(D_{21}^*\Delta w_{1b} - \Delta w_{2b})\right] \end{matrix} = 0 \qquad \text{(B-14)}$$

Multiplying Equation B-14 by $\delta^{*-3} = (L/\delta)^3$, one can obtain the expression in terms of the Rayleigh numbers based on the characteristic length of the diffusion cell, L ($Ra_1 = \beta_1 g L^3/\nu D_{11}$ and $Ra_2 = \beta_2 g L^3/\nu D_{11}$)

$$\begin{matrix} (L/\delta)^3\, \mathrm{K}^6(D_{22}^* - D_{12}^* D_{21}^*) + \\ +a^2[Ra_1(D_{12}^*\Delta w_{2b} - D_{22}^*\Delta w_{1b}) + Ra_2(D_{21}^*\Delta w_{1b} - \Delta w_{2b})] \end{matrix} = 0 \qquad \text{(B-15)}$$

Finally, Equation B-15 can be rewritten as,

$$\delta^{*3} - \frac{\mathrm{K}^6(D_{12}^* D_{21}^* - D_{22}^*)}{a^2[Ra_1(D_{12}^*\Delta w_{2b} - D_{22}^*\Delta w_{1b}) + Ra_2(D_{21}^*\Delta w_{1b} - \Delta w_{2b})]} = 0 \qquad \text{(B-16)}$$

The critical wavenumber that minimizes the thickness of the layer (i.e. $\frac{\partial \delta^*}{\partial a} = 0$) is

$$a_c = \frac{\pi}{\sqrt{2}} \approx 2.221, \qquad \text{(B-17)}$$

which is the same that the classical result for the stress-free Rayleigh-Bénard convection [41]. The corresponding minimum (critical) thickness is

$$\delta_c^* = \frac{3\pi^{4/3}}{2^{2/3}} \Re\left[\left(\frac{D_{12}^* D_{21}^* - D_{22}^*}{[Ra_1(D_{12}^* \Delta w_{2b} - D_{22}^* \Delta w_{1b}) + Ra_2(D_{21}^* \Delta w_{1b} - \Delta w_{2b})]}\right)^{1/3}\right] \tag{B-18}$$

Equation B-17 indicates the minimum thickness of the unstable layer needed for the perturbations to grow according to the linear stability criterion.

APPENDIX C. Description of the flow animations

Movie#1 to Movie#3 show the animation of the isosurfaces of the vertical velocity component and of the contours of the mass fraction of component 1. The red and blue contours on the vertical plane of the cell indicate the initial concentrations of component 1. The initial conditions are those of Exp#1 reported by Mialdun et al. [13] (See Table 1).

The parameters used for Movie#1 are: (Type II solution) $D_{22}^* = 2.50$, $D_{12}^* = 1.28$, $D_{21}^* = -0.425$, $Ra_1 = 1.78 \cdot 10^8$, $Ra_2 = 9.47 \cdot 10^7$, $Sc = 1.32 \cdot 10^3$; Green isosurface, $v^* = 50$ (ascending flow); Yellow isosurface, $v^* = -50$ (descending flow); Initial time $t^* = 10^{-4}$; End time $t^* = 3.91 \cdot 10^{-2}$.

The parameters used for Movie#2 are: (Type III solution) $D_{22}^* = 0.575$, $D_{12}^* = -1.05$, $D_{21}^* = -0.50$; $Ra_1 = 3.56 \cdot 10^7$, $Ra_2 = 1.89 \cdot 10^7$, $Sc = 1.32 \cdot 10^3$; Green isosurface, $v^* = 100$ (ascending flow); Yellow isosurface, $v^* = -100$ (descending flow); Initial time $t^* = 10^{-4}$, End time $t^* = 3.91 \cdot 10^{-2}$.

The parameters used for Movie#3 are: (Type IV solution) $D_{22}^* = 1.08$, $D_{12}^* = -1.00$, $D_{21}^* = -0.325$; $Ra_1 = 3.56 \cdot 10^7$, $Ra_2 = 1.89 \cdot 10^7$, $Sc = 1.32 \cdot 10^3$; Green isosurface, $v^* = 60$ (ascending flow); Yellow isosurface, $v^* = -60$ (descending flow); Initial time $t^* = 10^{-4}$, End time $t^* = 3.91 \cdot 10^{-2}$.